

## Research Article

# The Electrode Materials of Supercapacitor Based on TiO<sub>2</sub> Nanorod/MnO<sub>2</sub> Ultrathin Nanosheet Core/Shell Arrays

Li Zhang <sup>1</sup>, Qiong Song,<sup>1</sup> Chunyan Wang,<sup>1</sup> Xianjun Liu,<sup>1</sup> Xiujuan Jiang,<sup>1</sup> and Jian Gong <sup>2</sup>

<sup>1</sup>College of Food Engineering, Jilin Engineering Normal University, Changchun, Jilin 130052, China

<sup>2</sup>Key Laboratory of Polyoxometalates Science of Ministry of Education, Northeast Normal University, Changchun, Jilin 130024, China

Correspondence should be addressed to Li Zhang; [english8336@163.com](mailto:english8336@163.com) and Jian Gong; [gongj823@nenu.edu.cn](mailto:gongj823@nenu.edu.cn)

Received 14 October 2020; Revised 21 October 2020; Accepted 15 November 2020; Published 2 December 2020

Academic Editor: Zhenyi Zhang

Copyright © 2020 Li Zhang et al. This is an open access article distributed under the Creative Commons Attribution License, which permits unrestricted use, distribution, and reproduction in any medium, provided the original work is properly cited.

A hierarchical structure of TiO<sub>2</sub> nanorod/MnO<sub>2</sub> ultrathin nanosheet core/shell nanocomposite arrays on a conductive substrate has been prepared by two facile steps of hydrothermal reaction and annealing progress, which serving as electrodes present great potential application for high-performance supercapacitors. By adjusting the concentration of precursor aqueous solution, it can be found that the thickness of the MnO<sub>2</sub> shell in the as-designed hierarchical electrode material can be facilely controlled. By comparison, the obtained TiO<sub>2</sub> nanorod/MnO<sub>2</sub> ultrathin nanosheet as an electrode material can achieve the best electrochemical performance in terms of the area-specific capacitance up to 34.79 mF/cm<sup>2</sup> from the cyclic voltammetry (CV) test at the scan rate of 5 mV/s. Furthermore, the composited electrode has also demonstrated good stability, with the capacitance retention rate of about 91% through the cycle experiment test after 1000 cycles.

## 1. Introduction

In recent years, nanomaterials have been extensively studied [1–3]. More and more electronic products and electric vehicles are coming into people's lives in the past decade, following the increased demand for electric energy storage systems. The electrochemical supercapacitor, as an excellent electric energy storage device, attracts extensive research interests [4–8], because of the good cycle stability and excellent reversibility, fast recharge capability, cleanliness and environmental friendliness, high power density, and so on.

Up to now, various materials, such as carbon-based materials [9–13], transition metal compound, including oxides or sulfides of single or binary transition metals, such as MnO<sub>2</sub>, Co<sub>3</sub>O<sub>4</sub>, TiO<sub>2</sub>, ZnO, Ni<sub>3</sub>S<sub>2</sub>, NiO, NiCo<sub>2</sub>O<sub>4</sub>, and ZnCo<sub>2</sub>O<sub>4</sub> [14–25], and conducting polymers [26–29], have been widely used as supercapacitor electrodes. Since carbon-based materials adopt an electric double-layer mech-

anism, the capacitance performance is relatively lower than that of Faradaic pseudocapacitance, which has become the main bottleneck in the practical application of such materials. By contrast, pseudocapacitors, also called Faradaic pseudocapacitors, based on transition metal compound and conductive polymers have aroused lots of research interest, mainly due to their favorable reversible and fast redox reactions [30, 31].

Among various metal oxides, manganese dioxide (MnO<sub>2</sub>) is a very important electrode material because of the low cost, abundant reserves, ease of synthesis, and environmental protection and other outstanding characteristics [32–35]; the most important is that MnO<sub>2</sub> has very high theoretical specific capacitance. However, the poor conductivity of manganese dioxide (<10<sup>-5</sup> S/cm) greatly affects its application in the field of energy storage, especially for supercapacitors. Therefore, many researches have been carried out to improve the pure conductivity and low practical capacitance of MnO<sub>2</sub>. It has been widely accepted that manganese dioxide

nanostructures with a high specific surface area can effectively improve the utilization ratio of active materials of  $\text{MnO}_2$ . Furthermore, designing hierarchical electrodes by combining carbon materials or transition metal compound is aimed at achieving higher conductivity and electrical performance. The capacitance performance of these manganese dioxide-based composite materials is better than that of single manganese dioxide.

In recent years, titanium dioxide ( $\text{TiO}_2$ ) is another potential electrode material in the development of capacitor materials [36, 37]. Benefiting from the low cost, low toxicity, and abundant reserves, compared to  $\text{MnO}_2$ ,  $\text{TiO}_2$  possesses higher conductivity and electrochemical stability. In this work, we have prepared a hierarchical structure of the  $\text{TiO}_2$  nanorod/ $\text{MnO}_2$  ultrathin nanosheet core/shell nanocomposite on the FTO substrate (as a current collector) directly through two facile steps of hydrothermal reaction and annealing progress, and the binder-free of the obtained electrode avoids the morphology damage, the pore blockage, and the reduced conductivity of electrode materials, which is favorable for the electrochemical behavior. Meanwhile, it should be noted that the favorable electrode architecture design of conductive FTO as the current collector decorated by the hierarchical structure of the  $\text{TiO}_2$ / $\text{MnO}_2$  core/shell nanocomposite can achieve rapid ion and electron migration reactions simultaneously due to the structure of the vertical array and the porous abundance, which enhanced the activity of the electrode, thereby reducing internal resistance and improving capacitor performance. Finally, we have studied the electrochemical properties of materials, which also presented good capacitive properties in terms of high capacitance, low internal resistance, good rate capability, and long cycling stability, presenting great potential application for supercapacitors.

## 2. Experiment

**2.1. Materials.** The analytical grade reagents, tetrabutyl titanate ( $\text{C}_{16}\text{H}_{36}\text{O}_4\text{Ti}$ ), concentrated hydrochloric acid (HCl), potassium permanganate ( $\text{KMnO}_4$ ), sodium sulfate ( $\text{Na}_2\text{SO}_4$ ), and acetone ( $\text{C}_3\text{H}_6\text{O}$ ) were all purchased from Shanghai Chemical Reagent Company, and all of the water in our experiment is deionized water. The FTO conductive glass was purchased from Wuhan Jingge Solar Technology Co., Ltd., and the pretreatment of the FTO conductive glass was based on our previous report [38].

**2.2. The First Step of the Preparation:  $\text{TiO}_2$  Nanocore Array.** Rutile  $\text{TiO}_2$  was prepared with a simple hydrothermal reaction progress based on the literature [39]; in our experiment, the conductive glass of FTO was used as the electrode substrate, on which the electrode materials were grown. Specific experiment is described as follows for deionized water, concentrated hydrochloric acid, and tetrabutyl titanate, with a volume ratio of 30:30:1, first, mix equal volumes of deionized water and concentrated hydrochloric acid together, under magnetic stirring, and then add tetrabutyl titanate into the above mixture drop by

drop with vigorous stirring. 20 minutes later, the mixture was transferred into an autoclave (Teflon-lined), in which the FTO collector was placed vertically, and then, the reactor was sealed and maintained at  $150^\circ\text{C}$  for 4 h, cooling down naturally. Finally, take out the FTO substrate which has been covered with the obtained  $\text{TiO}_2$  nanorod arrays, wash them with deionized water and alcohol by turns for several times, and dry them naturally.

**2.3. The Next Step of the Preparation: The Shell of the  $\text{MnO}_2$  Ultrathin Nanosheet.** The final product of the  $\text{TiO}_2$  nanorod/ $\text{MnO}_2$  ultrathin nanosheet core/shell composite material was synthesized by the following second step of the hydrothermal process, the  $\text{TiO}_2$  nanorod-modified electrode from the above step was placed into an autoclave (the specification is 15 mL), and then 10 mL of potassium permanganate aqueous solution with a given concentration was added. Then, transfer the reactor into an oven and keep it for 6 hours at  $160^\circ\text{C}$ , turn off the oven and let it cool down, rinse the electrode with ethanol and deionized water, and dry them in an oven for 8 h at  $60^\circ\text{C}$ .

For this step, three parallel experiments were carried out; with other conditions unchanged, the concentration of potassium permanganate aqueous solution was adjusted in the range of 0.03–0.09 M (0.03 M, 0.06 M, and 0.09 M, respectively). Finally, the dried products were annealed in a furnace at  $350^\circ\text{C}$  for 2 h, and the final product  $\text{TiO}_2$ / $\text{MnO}_2$  nanomaterial was obtained. The differences in the morphology and the electrochemical performance of the products were studied.

The schematic diagram of the preparation of  $\text{TiO}_2$ / $\text{MnO}_2$  core-shell structure composite materials is shown in Figure 1. In order to easily distinguish the three kinds of products, in the following, the products obtained at different  $\text{KMnO}_4$  concentrations were named as TMnO-1, TMnO-2, and TMnO-3, corresponding to 0.03 M, 0.06 M, and 0.09 M of  $\text{KMnO}_4$  aqueous solution, respectively.

**2.4. Characterization.** The morphology of the products was characterized by field emission scanning electron microscopy (Philip XL-30 ESEM FEG) with an X-ray energy-dispersive spectrometry (EDX) analyses, transmission electron microscopy (TEM) (Philips JEM-2010 at an acceleration voltage of 200 kV), and X-ray diffraction (XRD) (D/max 2200 PC spectrometer with a  $\text{Cu K}\alpha$  source).

**2.5. Electrochemical Testing.** Electrochemical Workstation CHI660d (Chenhua) was used to carry out the electrochemical experiments, with a standard three-electrode cell testing system, in which the obtained composite nanomaterials is the working electrode,  $\text{Ag}/\text{AgCl}$  is the reference electrode, and the platinum wire is the counter electrode. Electrochemical tests of cyclic voltammetry (CV), galvanostatic charge/discharge (GCD), and electrochemical impedance spectroscopy (EIS) were carried out. The electrolyte was 1.0 M  $\text{Na}_2\text{SO}_4$  aqueous solution. The CV tests were performed from  $-0.2$  to  $0.8$  V. The frequency range of the EIS test was from 0.01 Hz to 100 kHz at an AC voltage of 5 mV. The test area of all of the electrode materials is

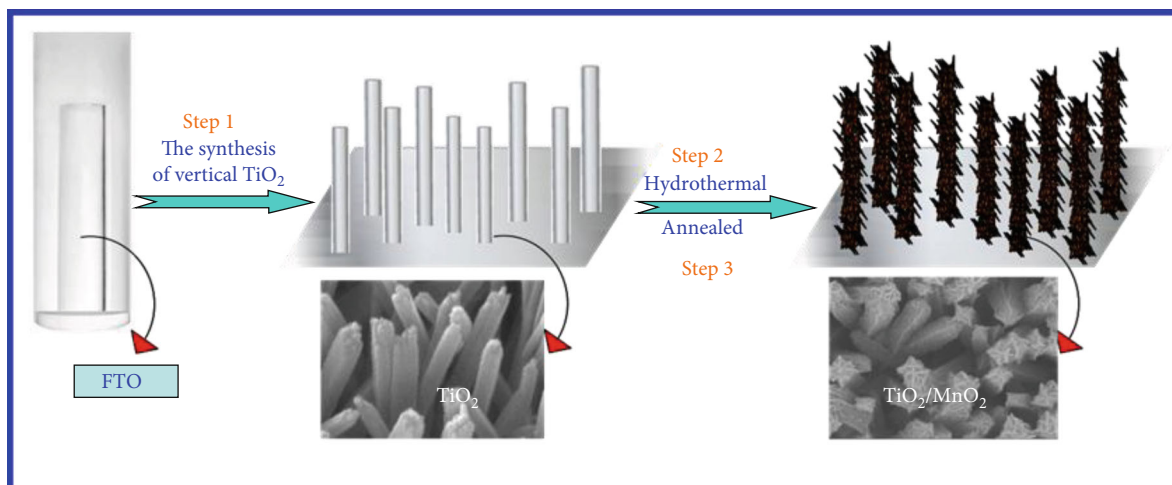


FIGURE 1: Schematic diagram of the preparation process of the  $\text{TiO}_2/\text{MnO}_2$  nanocomposite.

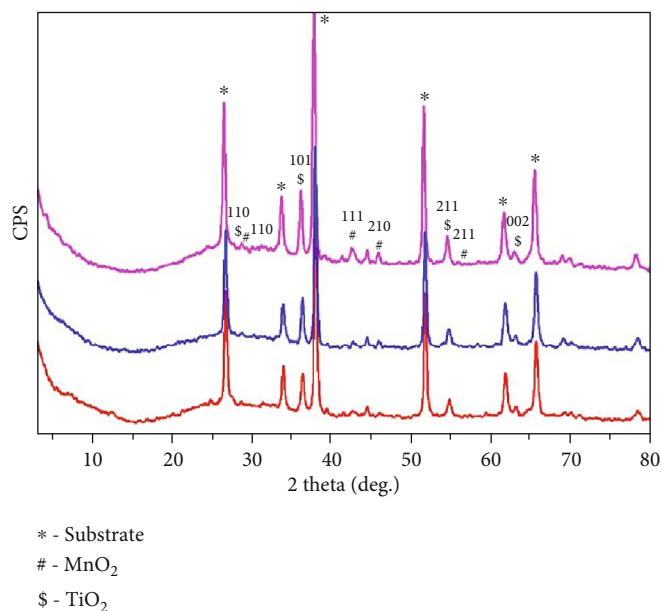


FIGURE 2: XRD patterns of  $\text{TiO}_2/\text{MnO}_2$  core-shell structure nanocomposite materials. TMnO-1 (red curve), TMnO-2 (blue curve), and TMnO-3 (purple curve).

$1 \times 1 \text{ cm}^2$ . The following formulation is used to calculate the area-specific capacitance of the product.

$$C_a = \frac{I \cdot t}{\Delta V \cdot S_i}, \quad (1)$$

$$C_a = \frac{\int I \cdot dv}{2(v \cdot \Delta V \cdot S)}. \quad (2)$$

In formula (1),  $C_a$  represents the area-specific capacitance,  $I$  represents the discharge current,  $t$  is the discharge time, and  $S_i$  represents the geometric area of the electrode, and in formula (2),  $\int I \cdot dv$  is the integral of the cyclic voltammetry curve area,  $v$  is the scanning speed of cyclic

voltammetry,  $S$  is the geometric area of the electrode, and  $\Delta V$  is the voltage window during scanning.

### 3. Results and Discussions

**3.1. XRD Spectra of the Products.** Figure 2 shows the three curves of XRD spectrum, respectively, representing the TMnO-1 (red curve), TMnO-2 (blue curve), and TMnO-3 (purple curve) obtained by our experiments. These materials were all directly tested on the FTO glass without any treatment. The symbol of star in the spectra represents the diffraction peak of the FTO glass base, which corresponds to No. 46-1088 in the standard JPCDS card. Among the three spectral curves, the diffraction peaks

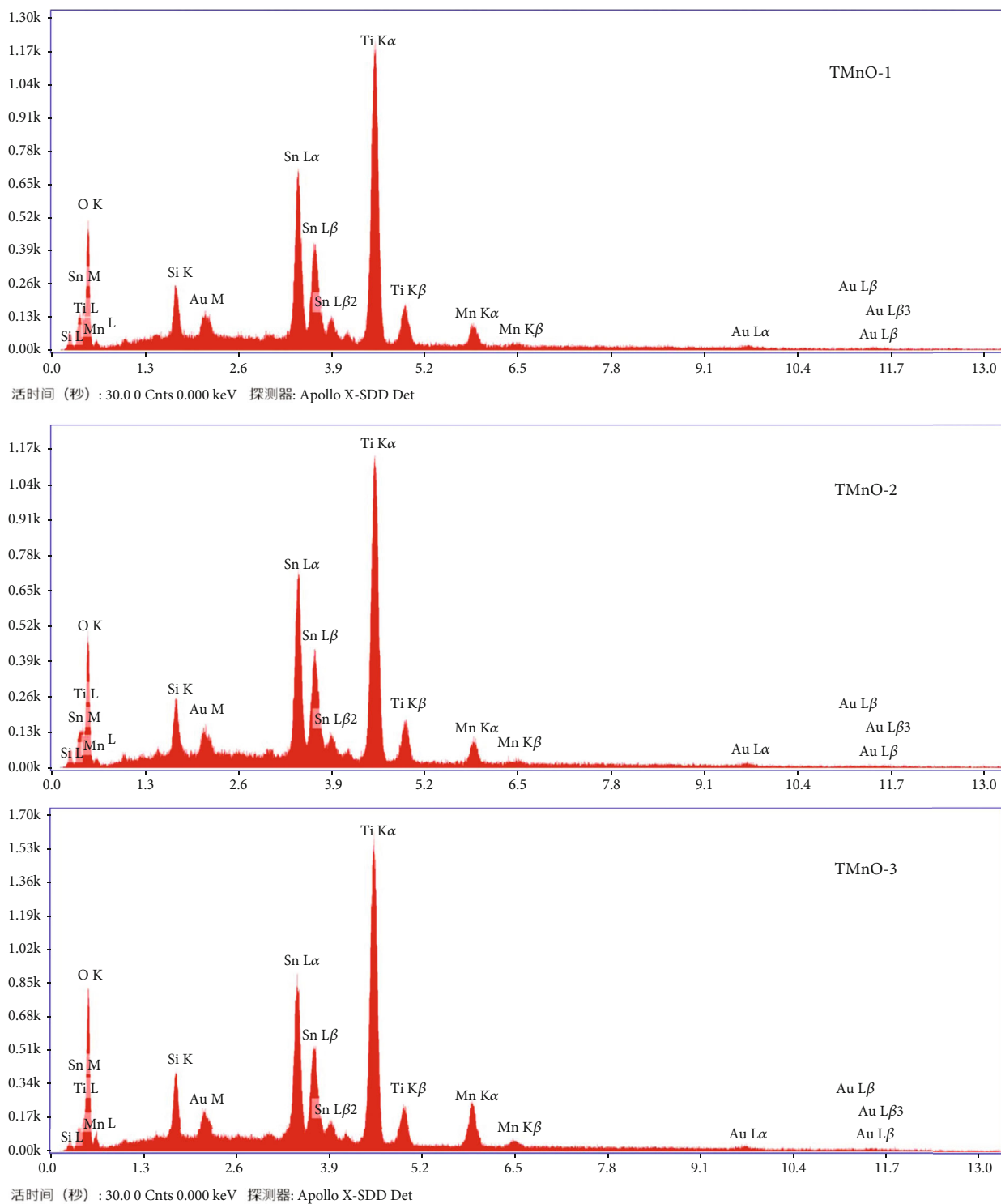


FIGURE 3: EDX of  $\text{TiO}_2/\text{MnO}_2$  core-shell structure composite materials. TMnO-1, TMnO-2, and TMnO-3.

corresponding to the # marks represent the (110), (111), (210), and (211) crystal planes of  $\text{MnO}_2$ . After analyzing the spectra, the crystalline of  $\text{MnO}_2$  corresponds to No. 81-2261 in the standard JCPDS cards, and the cell parameters are  $a = 4.404 \text{ \AA}$ ,  $b = 4.404 \text{ \AA}$ , and  $c = 2.876 \text{ \AA}$ , respectively. The \$ symbols can be attributed to the rutile  $\text{TiO}_2$ , and the cell parameters are  $a = 4.517 \text{ \AA}$ ,  $b = 4.517$

$\text{ \AA}$ , and  $c = 2.940 \text{ \AA}$ , respectively, corresponding to the standard card (JCPDS card No. 88-1175). Therefore, the XRD results exhibit that both  $\text{MnO}_2$  and  $\text{TiO}_2$  are presented in the three products.

**3.2. EDX Spectra of the Products.** The EDX spectra of TMnO-1, TMnO-2, and TMnO-3 are displayed in Figure 3. Except

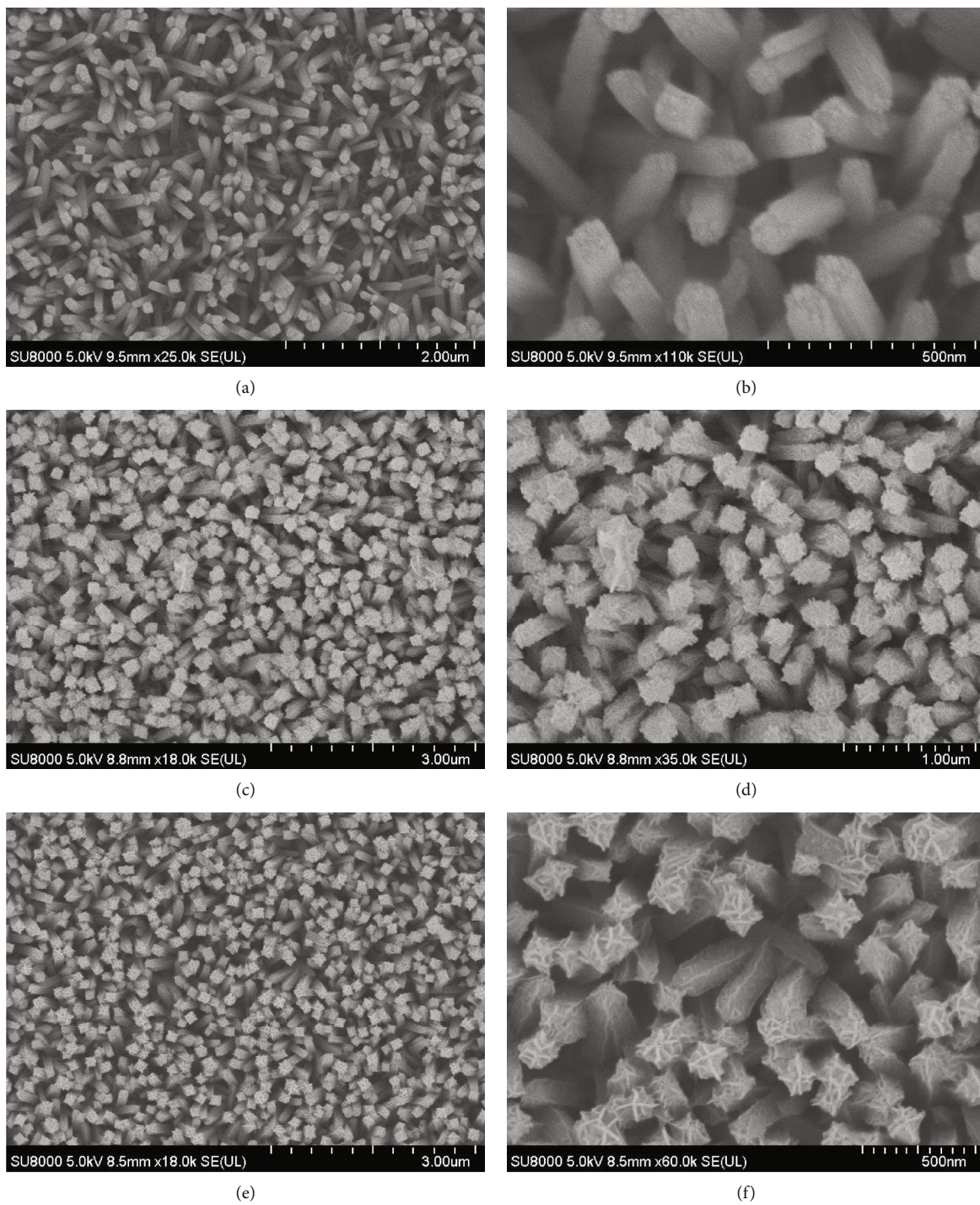


FIGURE 4: Continued.

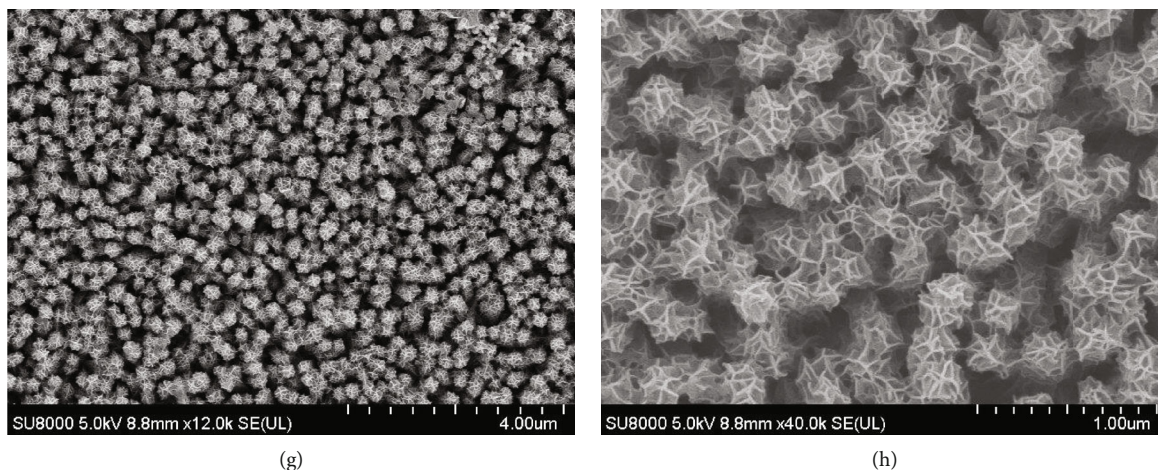


FIGURE 4: SEM images of  $\text{TiO}_2$  nanorods (a, b) prepared by the high-temperature hydrothermal method and  $\text{TiO}_2/\text{MnO}_2$  core-shell structure composite materials (TMnO-1 (c, d), TMnO-2 (e, f), and TMnO-3 (g, h)).

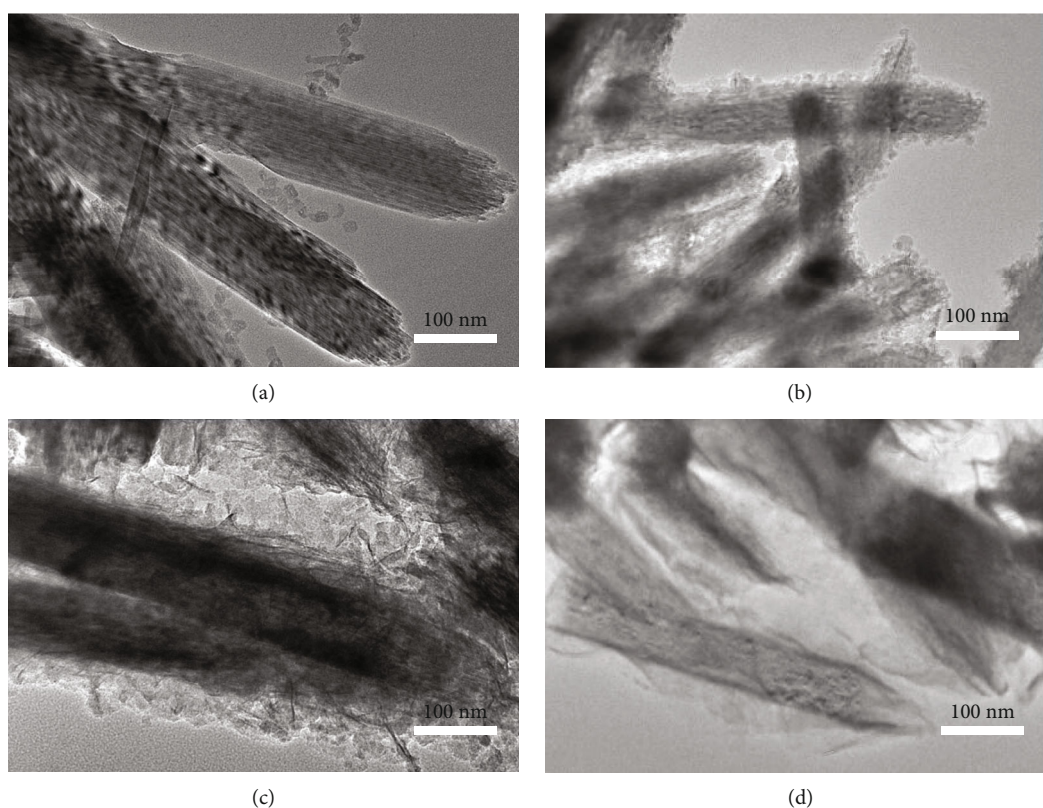


FIGURE 5: The TEM images of  $\text{TiO}_2$  nanorods (a) and core-shell structure of  $\text{TiO}_2/\text{MnO}_2$  composite materials: TMnO-1 (b), TMnO-2 (c), and TMnO-3 (d).

for the elements Sn and Si contained in the FTO glass, as well as the Au element contained in the sprayed gold, the existence of Ti, Mn, and O elements can further illustrate the coexistence of the two oxides of titanium dioxide and manganese dioxide in our as-synthesized products of  $\text{TiO}_2/\text{MnO}_2$  core-shell structure. At the same time, we can also observe that the content of the Mn element in the product increases obviously by increasing the concentration of potassium permanganate during the reaction, namely, high concentration

of the precursor, achieving high content of  $\text{MnO}_2$  in the product.

**3.3. SEM and TEM Photos of the Products.** Figures 4(a) and 4(b) are the SEM images of  $\text{TiO}_2$  prepared by the hydrothermal method at different magnifications.  $\text{TiO}_2$  arrays growing independently on the substrate can be seen, and the diameter is about 100 nm. Figures 4(c)–4(h) are the SEM images of TMnO-1, TMnO-2, and

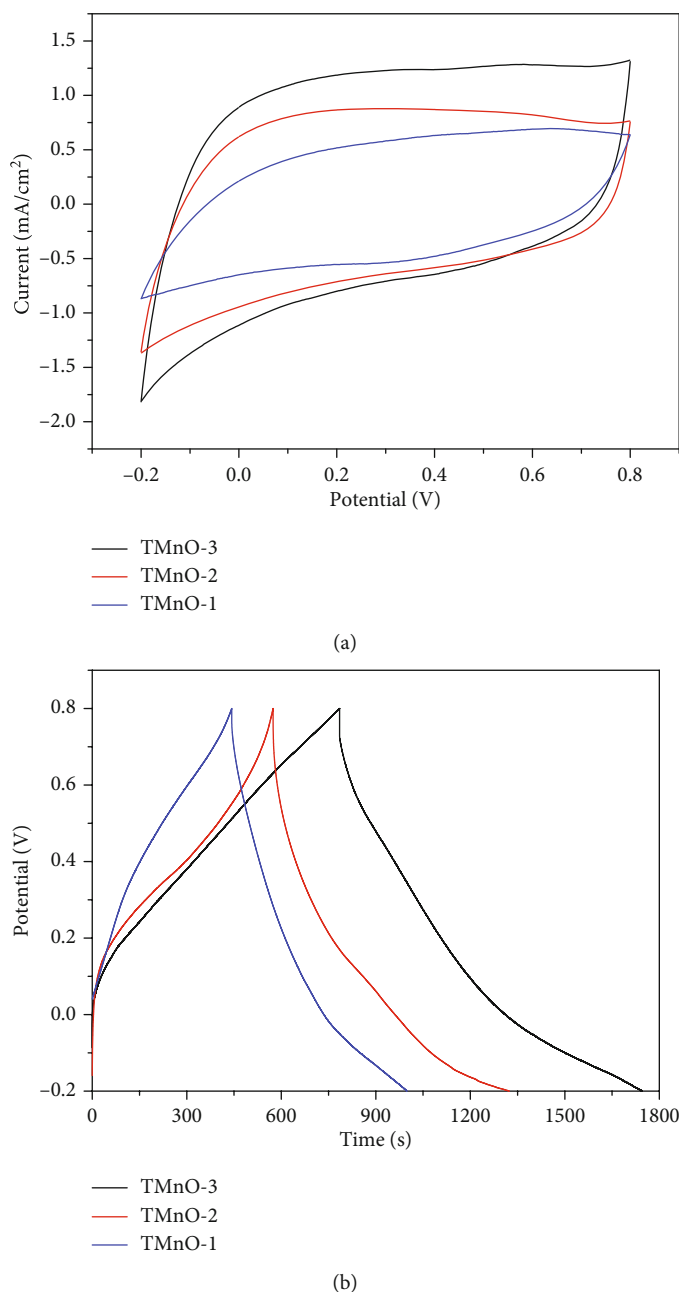


FIGURE 6: The CV curves (a) (at a scan rate of 100 mV/s) and GCD curves (b) (the current density of 0.03 mA/cm<sup>2</sup>) of TMnO-1 (black curve), TMnO-2 (red curve), and TMnO-3 (blue curve).

TMnO-3 at different magnifications, respectively. As the concentration of  $\text{KMnO}_4$  in the precursor solution increases, the thickness of the  $\text{MnO}_2$  shell wrapped around the  $\text{TiO}_2$  increases. Particularly, the net-like porous structure formed by the  $\text{MnO}_2$  sheet becomes more and more thick, and the original structure of the  $\text{TiO}_2$  array is still preserved well. Therefore, the resulting complex TMnO- $x$  ( $x = 1, 2, \text{ and } 3$ ) is the core-shell structure porous array.

Figure 5 shows the  $\text{TiO}_2$  nanorods prepared by the high-temperature hydrothermal method (Figure 5(a)) and the  $\text{TiO}_2/\text{MnO}_2$  core-shell structure composite materials TMnO-1, TMnO-2, and TMnO-3. Figure 5(a) is a pure  $\text{TiO}_2$  nanorod with a smooth surface and uniform diameter

of 100 nm. Figures 5(b)–5(d) are TEM images of TMnO-1, TMnO-2, and TMnO-3, respectively. The core-shell structure can be seen obviously, and  $\text{TiO}_2$  as the nanocore is covered with  $\text{MnO}_2$  homogeneously. The thickness of the  $\text{MnO}_2$  shell is obviously increased from TMnO-1 to TMnO-3. The large amount deposition of the  $\text{MnO}_2$  shell will improve the energy storage ability for the as-designed hierarchical electrode of  $\text{TiO}_2/\text{MnO}_2$  due to the increase in active sites.

### 3.4. Electrochemical Analysis

3.4.1. Cyclic Voltammetry (CV) and Galvanostatic Charge/Discharge (GCD). A series of the electrochemical tests

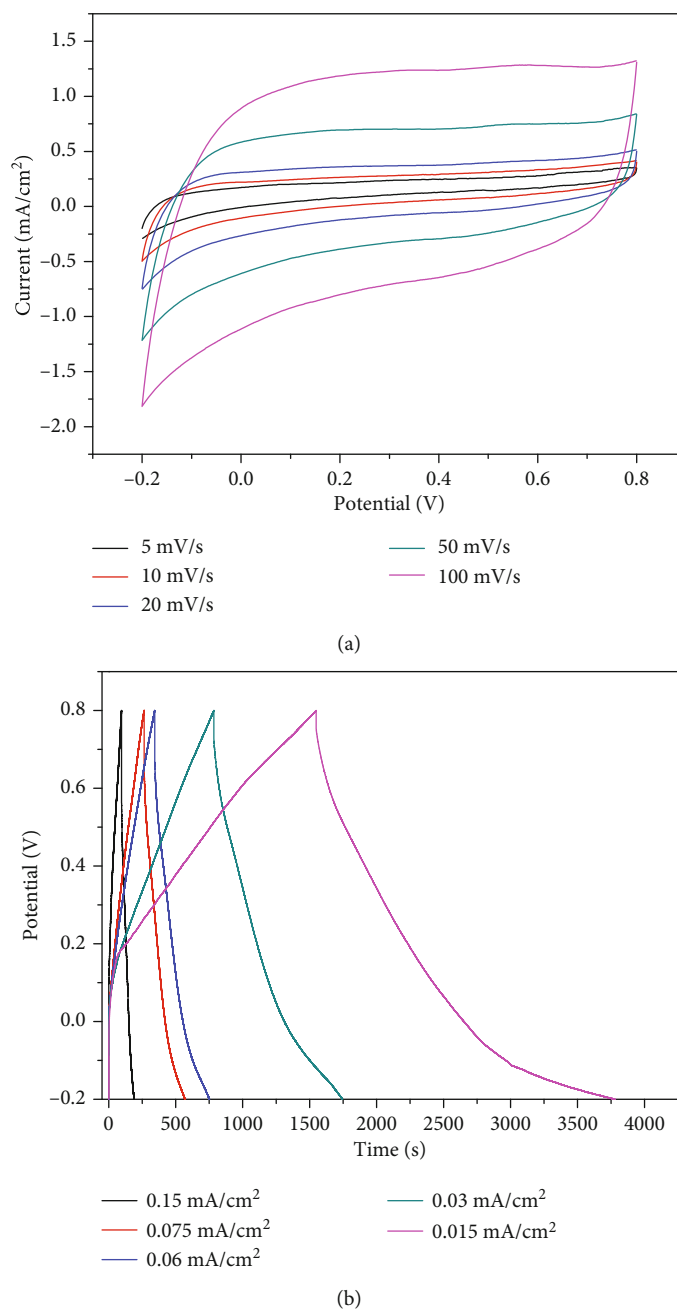
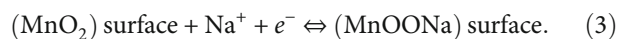


FIGURE 7: CV curves (at the scan rates from 5 to 100 mV/s) (a) and GCD curves of TMnO-3 at different current densities (from 0.15 mA/cm<sup>2</sup> to 0.015 mA/cm<sup>2</sup>) (b).

have been also conducted directly by using our devices without any treatment to investigate the electrochemical property of the products.

At a scan rate of 100 mV/s, a comparison diagram of CV results of the three kinds of products is shown in Figure 6(a). The black curve is TMnO-3, the red curve is TMnO-2, and the blue curve is TMnO-1. As can be seen from these curves, they all present a similar shape, in which a tiny redox peak appeared, indicating the pseudocapacitive characteristics of these materials. And they also have the characteristics of a double-layer capacitor. Meanwhile, it can be observed that TMnO-3 has the largest integrated area, indicating that this

material presents the best capacitive performance with the highest area capacitance among them. In the TMnO-*x* core-shell structure electrodes, the redox reaction (pseudocapacitance reaction) occurs between the valence states of Mn (IV) and Mn (III). Due to the insertion and extraction of Na<sup>+</sup> in the outer layer of MnO<sub>2</sub> [40, 41], the mechanism of the charge storage can be expressed by the following:



This mechanism indicates that the capacitance performance of the material mainly comes from MnO<sub>2</sub> through

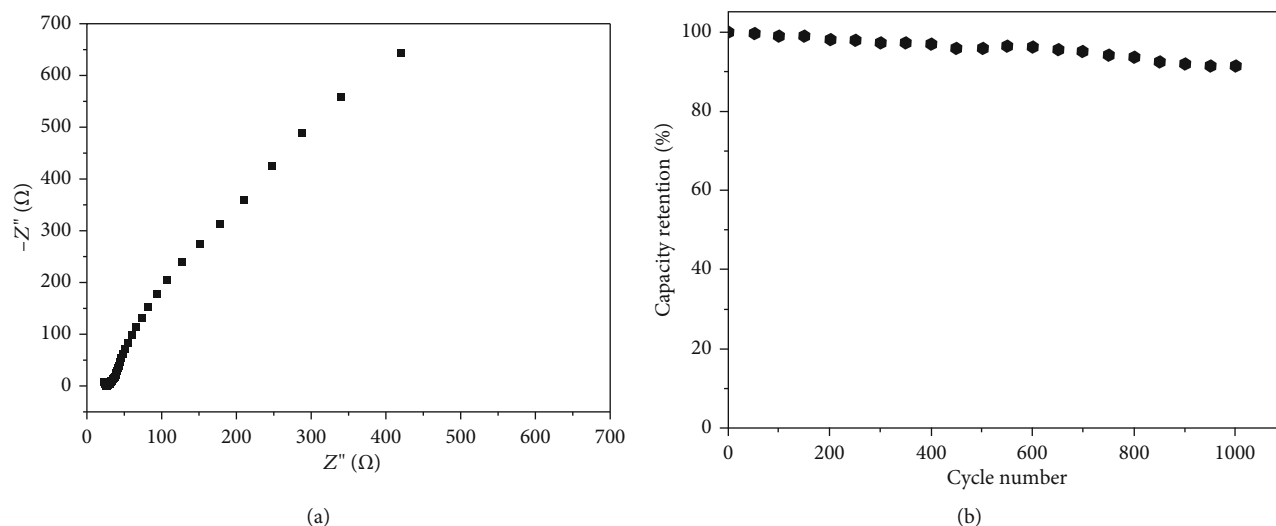


FIGURE 8: EIS spectrum of TMnO-3 (a) and the capacitance decay graph of TMnO-3 (at the current density of  $0.2 \text{ mA/cm}^2$  for 1000 charge-discharge cycles) (b).

the surface Faraday reaction (pseudocapacitive). In addition, the intercomponent synergy of  $\text{TiO}_2$  and  $\text{MnO}_2$  can further improve the performance of the composite materials. In the SEM and TEM pictures, the TMnO-3 possesses the most advantageous morphology, and hence, the surface  $\text{MnO}_2$  of TMnO-3 with more active sites can absorb more electrolyte ions. This result is consistent with the CV measurement result. At the same time, due to this special structure of core-shell arrays, the specific surface area increased and the diffusion path of the ions has been effectively reduced, which greatly increases the diffusion speed rate of the ions and accelerates the kinetics of the Faraday reaction.

Moreover, in addition to comparing the CV test results, the GCD tests were also performed for the series of  $\text{TiO}_2/\text{MnO}_2$  nanocomposites. The three curves in Figure 6(b) are the GCD curves of TMnO- $x$  at the current density of  $0.03 \text{ mA/cm}^2$ .

From the GCD test results, the compound of TMnO-3 exhibits the best electrochemical performance, which is consistent with the cyclic voltammetry tested above.

For the TMnO-3 serving as the supercapacitor electrode with the best capacitance effect, we also conducted a detailed electrochemical performance test on its capacitance. Figure 7(a) gives the CV curves of TMnO-3 at different scanning speeds, and Figure 7(b) shows the GCD curve of TMnO-3 under different current densities. By calculating from formula (2), the area-specific capacitance of TMnO-3 is up to  $34.79 \text{ mF/cm}^2$  at the scan rate of  $5 \text{ mV/s}$ . And from the GCD test, according to formula (1), the area-specific capacitance is  $28.87 \text{ mF/cm}^2$  at the current density of  $0.015 \text{ mA/cm}^2$ .

We conducted an electrochemical impedance test on TMnO-3, the purpose of which is to further study the property of our electrode material. The Nyquist plot of TMnO-3 is shown in Figure 8(a). In the high-frequency region, there is a semicircle with a smaller diameter, indicating that the charge transfer resistance is small in the product. At the same time, it can be observed that the slope of the curve in the low-

frequency region exceeds  $45^\circ$ , indicating a decrease in the diffusion resistance of the electrode. The impedance results once again demonstrate that TMnO-3 has good electrochemical performance.

Another important factor for judging the performance of a material whether with practical application value or not is its cycle stability. Figure 8(b) shows the test result of 1000 cycles of charge and discharge at a current density of  $0.2 \text{ mA/cm}^2$ . After the test, the capacitance of the TMnO-3 nanocomposite electrode material still remained 91%, indicating that the nanocomposite has good long cycle stability.

#### 4. Conclusion

We successfully prepared hierarchical core-shell arrays between  $\text{TiO}_2$  nanorods and  $\text{MnO}_2$  nanosheets, through two steps of simple low-cost hydrothermal progress and one step of the high-temperature annealing process. By adjusting the concentration of  $\text{KMnO}_4$  aqueous solution in the hydrothermal reaction progress, we obtained a series of hierarchical electrodes of  $\text{TiO}_2/\text{MnO}_2$  core-shell nanocomposites. And we discussed the different morphologies and electrochemical properties of these electrode materials, achieving the best product that has good properties. These results show that rationally designing a special structure of electrode material can result in better performance. Meanwhile, by combining different electrode materials together, benefiting from the synergistic interaction of the component, this contributes to increasing the electrochemical properties of energetic materials.

#### Data Availability

All of the data can be found in our manuscript.

#### Conflicts of Interest

There are no conflicts to declare.

## Acknowledgments

We gratefully acknowledge the Fund of PhD Research Initiation of Jilin Engineering Normal University (Nos. BSKJ201841 and BSKJ201923).

## References

- [1] Y. Liu, Z. Y. Zhang, Y. R. Fang et al., "IR-driven strong plasmonic-coupling on Ag nanorices/ $W_{18}O_{49}$  nanowires heterostructures for photo/thermal synergistic enhancement of  $H_2$  evolution from ammonia borane," *Applied Catalysis B: Environmental*, vol. 252, pp. 164–173, 2019.
- [2] D. P. Dong, C. X. Yan, J. D. Huang et al., "An electron-donating strategy to guide the construction of MOF photocatalysts toward co-catalyst-free highly efficient photocatalytic  $H_2$  evolution," *Journal of Materials Chemistry A*, vol. 7, no. 42, pp. 24180–24185, 2019.
- [3] N. Lu, M. H. Sun, X. M. Wei, P. Zhang, and Z. Y. Zhang, "Facile synthesis of lacunary Keggin-type phosphotungstates-decorated  $g-C_3N_4$  nanosheets for enhancing photocatalytic  $H_2$  generation," *Polymers*, vol. 12, no. 9, p. 1961, 2020.
- [4] T. S. Mathis, N. Kurra, X. H. Wang, D. Pinto, P. Simon, and Y. Gogotsi, "Energy storage data reporting in perspective guidelines for interpreting the performance of electrochemical energy storage systems," *Advanced Energy Materials*, vol. 9, no. 39, article 1902007, 2019.
- [5] H. Shao, Y. C. Wu, Z. Lin, P. L. Taberna, and P. Simon, "Nanoporous carbon for electrochemical capacitive energy storage," *Chemical Society Reviews*, vol. 49, no. 10, pp. 3005–3039, 2020.
- [6] A. Noori, M. F. El-Kady, M. S. Rahmanifar, R. B. Kaner, and M. F. Mousavi, "Towards establishing standard performance metrics for batteries, supercapacitors and beyond," *Chemical Society Reviews*, vol. 48, no. 5, pp. 1272–1341, 2019.
- [7] F. J. Miao, N. Lu, P. Zhang, Z. Y. Zhang, and G. S. Shao, "Multidimension-controllable synthesis of ant nest-structural electrode materials with unique 3D hierarchical porous features toward electrochemical applications," *Advanced Functional Materials*, vol. 29, no. 29, article 1808994, 2019.
- [8] Q. L. Wei, F. Y. Xiong, S. S. Tan et al., "Porous one-dimensional nanomaterials: design, fabrication and applications in electrochemical energy storage," *Advanced Materials*, vol. 29, no. 20, article 1602300, 2017.
- [9] F. J. Miao, C. L. Shao, X. H. Li, K. X. Wang, N. Lu, and Y. C. Liu, "Three-dimensional freestanding hierarchically porous carbon materials as binder-free electrodes for supercapacitors: high capacitive property and long-term cycling stability," *Journal of Materials Chemistry A*, vol. 4, no. 15, pp. 5623–5631, 2016.
- [10] F. J. Miao, C. L. Shao, X. H. Li et al., "Polyaniline-coated electrospun carbon nanofibers with high mass loading and enhanced capacitive performance as freestanding electrodes for flexible solid-state supercapacitors," *Energy*, vol. 95, pp. 233–241, 2016.
- [11] F. J. Miao, C. L. Shao, X. H. Li, K. X. Wang, N. Lu, and Y. C. Liu, "Freestanding hierarchically porous carbon framework decorated by polyaniline as binder-free electrodes for high performance supercapacitors," *Journal of Power Sources*, vol. 329, pp. 516–524, 2016.
- [12] M. F. El-Kady and R. B. Kaner, "Scalable fabrication of high-power graphene micro-supercapacitors for flexible and on-chip energy storage," *Nature Communications*, vol. 4, no. 1, pp. 1475–1483, 2013.
- [13] Q. Y. Yang, Z. Xu, B. Fang et al., "MXene/graphene hybrid fibers for high performance flexible supercapacitors," *Journal of Materials Chemistry A*, vol. 5, no. 42, pp. 22113–22119, 2017.
- [14] Q. Y. Liao, N. Li, S. X. Jin, G. W. Yang, and C. X. Wang, "All-solid-state symmetric supercapacitor based on  $Co_3O_4$  nanoparticles on vertically aligned graphene," *ACS Nano*, vol. 9, no. 5, pp. 5310–5317, 2015.
- [15] D. P. Cai, H. Huang, D. D. Wang et al., "High-performance supercapacitor electrode based on the unique  $ZnO@Co_3O_4$  core/shell heterostructures on nickel foam," *ACS Applied Materials & Interfaces*, vol. 6, no. 18, pp. 15905–15912, 2014.
- [16] Y. Zhao, L. F. Hu, S. Y. Zhao, and L. M. Wu, "Preparation of  $MnCo_2O_4@Ni(OH)_2$  core-shell flowers for asymmetric supercapacitor materials with ultrahigh specific capacitance," *Advanced Functional Materials*, vol. 26, no. 23, pp. 4085–4093, 2016.
- [17] X. Y. Liu, S. J. Shi, Q. Q. Xiong et al., "Hierarchical  $NiCo_2O_4@NiCo_2O_4$  core/shell nanoflake arrays as high-performance supercapacitor materials," *ACS Applied Materials & Interfaces*, vol. 5, no. 17, pp. 8790–8795, 2013.
- [18] S. Chen, M. Y. Zhang, G. Jiang, Z. Y. Zhang, and X. J. Zhou, " $NiMoO_4$  nanorods@hydrous  $NiMoO_4$  nanosheets core-shell structured arrays for pseudocapacitor application," *Journal of Alloys and Compounds*, vol. 814, article 152253, 2020.
- [19] S. Chen, M. Y. Zhang, X. Z. Ma, L. Li, X. J. Zhou, and Z. Y. Zhang, "Asymmetric supercapacitors by integrating high content  $Na^+/K^+$ -inserted  $MnO_2$  nanosheets and layered  $Ti_3C_2Tx$  paper," *Electrochimica Acta*, vol. 332, p. 135497, 2020.
- [20] J. J. Shen, X. C. Li, L. Wan et al., "An asymmetric supercapacitor with both ultra-high gravimetric and volumetric energy density based on 3D  $Ni(OH)_2/MnO_2@$  carbon nanotube and activated polyaniline-derived carbon," *ACS Applied Materials & Interfaces*, vol. 9, no. 1, pp. 668–676, 2016.
- [21] Y. Chen, W. K. Pang, H. Bai et al., "Enhanced structural stability of nickel-cobalt hydroxide via intrinsic pillar effect of meta-borate for high-power and long-life supercapacitor electrodes," *Nano Letters*, vol. 17, pp. 429–436, 2016.
- [22] X. F. Lu, X. Y. Chen, W. Zhou, Y. X. Tong, and G. R. Li, " $\alpha-Fe_2O_3@PANI$  core-shell nanowire arrays as negative electrodes for asymmetric supercapacitors," *ACS Applied Materials & Interfaces*, vol. 7, no. 27, pp. 14843–14850, 2015.
- [23] W. Du, Y. L. Bai, J. Q. Xu et al., "Advanced metal-organic frameworks (MOFs) and their derived electrode materials for supercapacitors," *Journal of Power Sources*, vol. 402, pp. 281–295, 2018.
- [24] J. S. Zhao, Y. Tian, A. F. Liu, L. Song, and Z. S. Zhao, "The NiO electrode materials in electrochemical capacitor: a review," *Materials Science in Semiconductor Processing*, vol. 96, pp. 78–90, 2019.
- [25] S. H. Ji, N. R. Chodankar, W. S. Jang, and D. H. Kim, "High mass loading of  $h-WO_3$  and  $\alpha-MnO_2$  on flexible carbon cloth for high-energy aqueous asymmetric supercapacitor," *Electrochimica Acta*, vol. 299, pp. 245–252, 2019.
- [26] F. J. Miao, C. L. Shao, X. H. Li et al., "Flexible solid-state supercapacitors based on freestanding electrodes of electrospun polyacrylonitrile@polyaniline core-shell nanofibers," *Electrochimica Acta*, vol. 176, pp. 293–300, 2015.

- [27] T. Y. Liu, L. Finn, M. H. Yu et al., "Polyaniline and polypyrrole pseudocapacitor electrodes with excellent cycling stability," *Nano Letters*, vol. 14, no. 5, pp. 2522–2527, 2014.
- [28] L. Wang, L. Chen, B. Yan et al., "In situ preparation of SnO<sub>2</sub>@-polyaniline nanocomposites and their synergetic structure for high-performance supercapacitors," *Journal of Materials Chemistry A*, vol. 2, no. 22, pp. 8334–8341, 2014.
- [29] K. Wang, H. P. Wu, Y. N. Meng, and Z. X. Wei, "Conducting polymer nanowire arrays for high performance supercapacitors," *Small*, vol. 10, no. 1, pp. 14–31, 2014.
- [30] X. Lu, J. F. Zhu, W. L. Wu, and B. Zhang, "Hierarchical architecture of PANI@TiO<sub>2</sub>/Ti<sub>3</sub>C<sub>2</sub>T<sub>x</sub> ternary composite electrode for enhanced electrochemical performance," *Electrochim Acta*, vol. 228, pp. 282–289, 2017.
- [31] Z. H. Li, M. F. Shao, L. Zhou et al., "A flexible all-solid-state micro-supercapacitor based on hierarchical CuO@layered double hydroxide core-shell nanoarrays," *Nano Energy*, vol. 20, pp. 294–304, 2016.
- [32] Y. Huang, Y. Huang, W. Meng et al., "Enhanced tolerance to stretch induced performance degradation of stretchable MnO<sub>2</sub>-based supercapacitors," *ACS Applied Materials & Interfaces*, vol. 7, no. 4, pp. 2569–2574, 2015.
- [33] J. P. Liu, J. Jiang, M. Bosman, and H. J. Fan, "Three-dimensional tubular arrays of MnO<sub>2</sub>-NiO nanoflakes with high areal pseudocapacitance," *Journal of Materials Chemistry*, vol. 22, no. 6, pp. 2419–2426, 2012.
- [34] Q. Li, Z. L. Wang, G. R. Li, R. Guo, L. X. Ding, and Y. X. Tong, "Design and synthesis of MnO<sub>2</sub>/Mn/MnO<sub>2</sub> sandwich-structured nanotube arrays with high supercapacitive performance for electrochemical energy storage," *Nano Letters*, vol. 12, no. 7, pp. 3803–3807, 2012.
- [35] Z. M. Li, Y. F. An, Z. G. Hu et al., "Preparation of a two-dimensional flexible MnO<sub>2</sub>/graphene thin film and its application in a supercapacitor," *Journal of Materials Chemistry A*, vol. 4, no. 27, pp. 10618–10626, 2016.
- [36] Y. Yang, D. Kim, M. Yang, and P. Schmuki, "Vertically aligned mixed V<sub>2</sub>O<sub>5</sub>-TiO<sub>2</sub> nanotube arrays for supercapacitor applications," *Chemical Communications*, vol. 47, no. 27, pp. 7746–7748, 2011.
- [37] B. Pant, M. Park, and S. J. Park, "TiO<sub>2</sub> NPs assembled into a carbon nanofiber composite electrode by a one-step electrospinning process for supercapacitor applications," *Polymers*, vol. 11, no. 5, pp. 899–902, 2019.
- [38] L. Zhang, L. Chen, S. X. Liu, J. Gong, Q. Tang, and Z. M. Su, "Honeycomb-patterned hybrid films of surfactant-encapsulated polyoxometalates by a breath figure method and its electrocatalysis for BrO<sub>3</sub><sup>-</sup>," *Dalton Transactions*, vol. 47, no. 1, pp. 105–111, 2018.
- [39] B. Liu and E. S. Aydil, "Growth of oriented single-crystalline rutile TiO<sub>2</sub> nanorods on transparent conducting substrates for dye-sensitized solar cells," *Journal of the American Society*, vol. 131, no. 11, pp. 3985–3990, 2009.
- [40] M. Toupin, T. Brousse, and D. Bélanger, "Charge storage mechanism of MnO<sub>2</sub> electrode used in aqueous electrochemical capacitor," *Chemistry of Materials*, vol. 16, no. 16, pp. 3184–3190, 2004.
- [41] G. P. Xiong, K. P. S. S. Hembram, R. G. Reifengerger, and T. S. Fisher, "MnO<sub>2</sub>-coated graphitic petals for supercapacitor electrodes," *Journal of Power Sources*, vol. 227, pp. 254–259, 2013.